CTRC Research Publications   Cooling Technologies Research Center

2013

Review of Molten-Salt Thermocline Tank Modeling for Solar Thermal Energy Storage

S. M. Flueckiger
Purdue University

Z. Yang
Tsinghua University

S V. Garimella
Purdue University, sureshg@purdue.edu

Follow this and additional works at: https://docs.lib.purdue.edu/coolingpubs

Design of Molten-Salt Thermocline Tanks for Solar Thermal Energy Storage[*]

Zhen Yang[1], Scott M. Flueckiger[2], and Suresh V. Garimella[2**]

[1]Key Laboratory for Thermal Science and Power Engineering of Ministry of Education

Department of Thermal Engineering

Tsinghua University

Beijing 100084 China

[2]School of Mechanical Engineering

Cooling Technologies Research Center, an NSF IUCRC

585 Purdue Mall, Purdue University

West Lafayette, IN 47907-2088 USA

[**] Author to whom correspondence should be addressed: (765) 494-5621, sureshg@purdue.edu

Abstract

Molten-salt thermocline tanks are a low-cost option for thermal energy storage in concentrating solar power (CSP) systems. A review of previous molten-salt thermocline tank studies is performed to identify key issues associated with tank design. Discharge performance improves with both larger tank height and smaller internal filler diameter due to increased thermal stratification and sustained outflow of molten salt with high thermal quality. For well-insulated (adiabatic) tanks, low molten-salt flow rates reduce the axial extent of the heat-exchange region and increase discharge efficiency. Under non-adiabatic conditions, low flow rates become detrimental to stratification due to the development of recirculation zones inside the tank. For such tanks, higher flow rates reduce molten-salt residence time inside the tank and improve discharge efficiency. Despite the economic advantages of a thermocline tank, thermal ratcheting of the tank wall remains a significant design concern. The potential for thermal ratcheting is reduced through the inclusion of an internal insulation layer between the molten salt and tank wall.

Keywords: concentrating solar thermal power, thermocline tank, molten salt

1. Concentrating Solar Power (CSP) Technologies

Diminishing fossil fuel reserves and increasing effects of anthropogenic climate change due to greenhouse gas emissions have led to an unprecedented global interest in renewable sources of energy. A leading candidate among these emerging technologies is the conversion of sunlight to electricity. This process can be achieved either directly with solar cells (using the photovoltaic effect) or indirectly by concentration of incident solar radiation to generate high-grade heat that then supports steam generation in a traditional Rankine cycle. For electricity generation at a large commercial scale, concentrating solar power (CSP) is the most economical conversion process. In a CSP plant, solar energy is concentrated via large arrays of mirrors which focus sunlight onto a heat transfer fluid (HTF) that is then pumped to the power block. To maximize the energy conversion, plants should be constructed in areas with direct solar radiation of at least 1800 kWh/m^2/year [1]. North Africa, the Middle East, as well as the Mojave Desert located in the southwest United States offer excellent sites.

Existing CSP technologies are categorized into four main solar harvesting methods: parabolic trough, central receiver, linear Fresnel reflector, and Stirling dish receiver. In a parabolic trough system, curved mirrors are organized around a tubing network filled with a HTF. To maximize daily concentration, the mirrors are typically operated on a north-south axis tracker to follow the change in solar azimuth angle. As the HTF is heated by the reflected sunlight, losses develop from convection and emissive radiation to the surroundings. The losses are dampened by coating the absorber tubes with wavelength-selective paints and encasing them in vacuum glass jackets. Commercial examples of parabolic trough design include the nine Solar Electric Generating Systems (SEGS) plants constructed by Luz International between 1985 and 1991 in the Mojave Desert. Using synthetic oil as the HTF, these plants achieve receiver

temperatures up to 390 °C and annual energy outputs of 30,100 MWh in SEGS I up to 256,125 MWh in SEGS IX. Still in operation, the combined electrical output of these systems is 354 MW_e. As of 2010, other notable parabolic plants include the 65 MW_e Nevada Solar One and the ANDASOL 1 and 2 plants in Spain which provide a combined output of 100 MW_e.

In contrast to a parabolic trough, a central-receiver or power tower concentrator uses thousands of individual mirrors known as heliostats to focus sunlight onto a single zone at the top of a tower. The HTF is pumped across this zone to absorb the heat and carry it to the power block. Each heliostat is a two-axis tracker that rotates in both the azimuth and altitude directions. The combined effect is an increased concentrated heat flux relative to parabolic troughs, allowing for higher receiver temperatures and increased thermodynamic efficiencies in the power block. As the HTF is only heated at a single point in a central receiver, an extensive tubing network is not required. However, the lack of a traditional HTF suitable for the higher temperature operation has largely limited the central-receiver design to experimental plants. Such plants include the historic Solar One (distinct from the Nevada Solar One plant) and Solar Two systems commissioned by the US Department of Energy in Barstow, California. Solar One was constructed with 1818 heliostats and successfully operated from 1982 to 1988 with a design output of 10 MW_e. To make use of the higher receiver temperatures, Solar One applied direct steam generation (DSG) in which water acted as the HTF, heated up to 516 °C [2]. While this eliminated the need for heat exchangers between the collection system and the power block, containment of the superheated water required high-pressure tubing lines. After decommissioning, this plant site was retrofitted with additional heliostats and converted to the Solar Two plant and operated from 1995 to 1999. The first commercial central-receiver plant is the PS10 plant located in Seville, Spain with a current output of 11 MW_e.

A linear Fresnel reflector is a potentially cheaper alternative [3] to parabolic trough designs in which a continuous curved mirror is replaced with a series of flat mirrors. Placing these individual mirrors at equal elevation, each mirror is adjusted to a different angular orientation in order to approximate the parabolic trough behavior. Cost savings arise from the ability to use flat mirrors and the reduced wind load with installation near the ground. Existing Fresnel plants are so far limited to less than 5 MW_e output, but offer promise for further development.

In contrast to the array design of the parabolic trough and Fresnel reflector, a Stirling dish receiver [4] requires only a single, curved two-axis reflector. A Stirling engine is positioned at the focal point of the two-axis dish receiver to convert the concentrated solar energy to rotational energy for a generator. As a Stirling engine uses a gas as the working fluid, elevated receiver temperatures are sustained to achieve very high conversion efficiencies. However, the use of a single paraboloidal reflector in conjunction with a Stirling engine limits the individual unit size and requires dish receivers to be operated collectively to supply larger amounts of electricity.

2. Energy Storage Overview

While solar energy can be successfully converted to electricity at a commercial scale, a significant performance constraint is the constant variation of sunlight due to the Earth's rotation and random cloud transients. As a consequence of nighttime conditions, CSP operations are forced to undergo daily startup and shutdown operations. In addition, daily cloud transients sporadically reduce solar irradiance during daytime plant operation and lead to intermittent decreases in output. Fossil fuel-based or other backup generation is required to maintain consistent generation, independent of solar conditions. This need for fossil-fuel backup

diminishes the renewable and environmental aspects of the CSP plant. One remedy is to generate excess power at peak insolation and store a portion of the output; later dispatched during periods of insufficient insolation. An over-designed collection area is necessary if the storage process intends to extend the period of daily output in addition to accommodating cloud transients [5]. While adding some installation and maintenance cost, storage is essential for improving the performance of CSP plants to better replicate that of fossil-fuel power plants.

In a CSP plant, energy storage can be installed at three separate locations relative to the thermodynamic power cycle: downstream of the cycle, within the cycle, and upstream of the cycle. Storage downstream of the cycle is achieved by generating an excess amount of electricity that is then stored in some form of a capacitor for later use. Due to limitations in existing technology (such as economical battery storage) this type of storage has not been developed for large-scale, power plant applications.

Within the power cycle, excess steam can be generated in the boiler and stored in a pressure vessel known as a steam accumulator. While a proven technology, accumulators require both high-strength walls and large thermal insulation to maintain the desired steam conditions. Such accumulators are included in the PS10 central-receiver plant in Spain, which provide one hour of storage capability.

To avoid storing high-pressure steam, an excess amount of hot HTF can be generated from the solar collector system to maintain a high-temperature reservoir instead. The process is known as thermal energy storage (TES) and has garnered significant interest in recent years. A significant advantage is the availability of design options inherent to TES systems, through the choice of different materials, processes, and installations, as discussed below.

3. Thermal Energy Storage Processes

TES technologies exploit one or more of three distinct mechanisms: thermochemical storage, latent heat storage, and sensible heat storage. In thermochemical storage, the elevated temperature of the HTF is used to promote a reversible endothermic reaction. The absorbed thermal energy is stored as chemical bonds within the reaction products. When the energy must be recovered, the reverse exothermic process is induced through catalysis [5]. In order for a given reaction process to be suitable for a CSP plant, the reaction temperatures must be comparable to the operational range of the HTF. Lovegrove *et al*. [6] investigated the potential for the closed-loop conversion of ammonia as a potential storage system for dish-receivers. In operation, liquid ammonia enters the solar collector and is converted to nitrogen and hydrogen gas. The reaction products are sent to a separation chamber to remove any remaining ammonia from the gas. To retrieve the heat, the gases are sent from the separation chamber to the power block to undergo the exothermic conversion to liquid ammonia and returned to the separation chamber. Based on experimental studies and reaction simulations, a storage efficiency of 52% is obtainable, although large pressures are required to maintain liquefied ammonia at the elevated temperatures. Chemical storage remains in the early stages of development due to the design complexities and costs involved at a commercial scale.

As an alternative to chemical conversion, heat from the HTF can be used to induce a phase change in a single material to isothermally store energy at the transition temperature. This avoids large pressure gradients as the selected phase change material (PCM) undergoes a solid-liquid transition. The energy storage associated with this transition is proportional to the heat of fusion of the PCM. As with chemical storage, the transition temperature of the PCM must be within the temperature variation of the HTF.

7

While latent heat systems typically require much lower storage volume relative to other mechanisms, the low thermal conductivities associated with PCMs impede the rate of energy transfer. To resolve this material deficiency, PCMs are either encapsulated in a packed bed to increase surface area or combined with high-conductivity metal foams to improve overall thermal diffusion. Regin *et al*. [7] simulated a packed bed filled with encapsulated PCM (paraffin wax) to investigate latent heat storage for solar water heaters. Energy transfer between the water and the bed was solved using the one-dimensional Schumann equations while phase change of the PCM was analyzed with the enthalpy method. As expected, the simulation revealed that reduced capsule size increased the melting rate due to the increased surface area to volume ratio. However, heat transfer with the solid-phase PCM was much slower than that with the liquid phase, leading to excessive charging times for the storage system.

For metal foam enhancement of bulk PCM, simulations have typically been performed under the assumption of thermal equilibrium between the PCM and the metal foam, and constant material properties. As the thermal diffusivities of the PCM and foam are often significantly different, these temperatures cannot always be assumed equal. Krishnan *et al*. [8] eliminated the thermal equilibrium assumption by developing a two-temperature finite volume model for phase change within the porous foam. A two-temperature model solves separate energy equations for the PCM and the foam, coupled by an interstitial Nusselt number. The result is co-located data storage with two temperatures recorded at each cell of the discretized domain. The interstitial Nusselt number for the liquid phase was determined with the correlation by Wakao and Kaguei [9] based on natural convection in the melt region. For transfer from the foam to solid PCM, the Nusselt number was obtained from the diffusive limit of the correlation. From a parametric study, thermal equilibrium was found to be a valid assumption only for interstitial Nusselt

numbers greater than 5.9. Yang and Garimella [10] extended this modeling work to include density change of the PCM during phase change. The effect of including volume shrinkage in the PCM into the simulation was to increase the melting rate, while volume expansion slowed the phase change process.

For CSP application, Laing *et al*. [11] investigated the use of latent heat within a three-component storage system for steam generation in the power block during short periods of low solar irradiance. The latent heat component was limited to steam generation in the power block, while the remaining two storage sections applied sensible heat via the thermal mass of concrete for preheating and superheating, respectively. A test module with heat exchanger tubes surrounded by the PCM was constructed to assess the latent heat performance using sodium nitrate ($NaNO_3$) as the PCM. Energy transfer improved with axial aluminum fins included along each of the heat exchanger tubes. The experimental setup was subjected to 172 phase change cycles and found to experience no degradation of the PCM or the fin interface.

In purely sensible heat storage, thermal energy in the HTF is used to heat a single-phase material to an elevated temperature, or is retained within an excess volume of HTF. The stored thermal energy is proportional to the heat capacity of the selected storage material and the temperature difference between hot and cold HTF. This storage mechanism avoids phase change, and both solid and liquid storage systems have been developed for CSP applications. In solid storage, a portion of the HTF is diverted from the solar collection system to flow through bulk material of large thermal mass. Laing *et al*. [12] simulated a solid thermal storage system composed of concrete, a low-cost storage material. Due to the low thermal conductivity of concrete, the HTF is pumped through a tube bank or register embedded in the concrete slab. The inclusion of axial fins and reinforcement grids in the slab improved the thermal performance of

the storage system but were found not to be cost effective. A 20 m^3 test module of the concrete and tube register design was later constructed for experimental analysis [13]. Using thermal oil as the HTF, the test module was successfully operated for nearly 100 cycles between 350 °C to 390 °C. From this testing, the heat capacity and storage efficiency were found to be 26.6 kWh/m^3 and 67%, respectively, under the given operating conditions. The low efficiency was attributed to the prototypical nature of the test module and was projected to increase up to 95% for a commercial system.

In contrast to previous methods, sensible liquid media storage is the most well understood and commercially proven storage technology. An overview of the design characteristics associated with liquid storage systems is provided in the following section.

4. Sensible Heat Storage in Liquids

The operation of a liquid media storage system in a CSP plant can be described in terms of system integration, storage design, and HTF selection. System integration refers to operation of the storage system relative to the solar collection system, and can employ either a direct or an indirect scheme. With indirect integration, the collector loop and the energy storage system are isolated from one another, with energy transfer between the two occurring through a heat exchanger. The two fluid volumes are not in contact, so that the collector HTF and the storage fluid need not be the same. In direct integration, the storage system is integrated within the collector loop such that the two sections are exposed to the same HTF. This method improves the efficiency of power generation as heat transfer and loss of thermal quality across a heat exchanger is avoided.

Two prevailing design options exist for both indirect and direct liquid thermal energy storage: two-tank storage and single-tank thermocline storage. In a two-tank storage system, the volumes of hot and cold liquid (typically, a molten salt) are maintained in separate tanks. For indirect storage, these tanks are connected by one side of the heat exchanger that is installed in the collection loop. The storage system is charged by transferring molten salt from the cold tank to the hot tank while absorbing heat from the hotter HTF in the intermediate heat exchanger. To discharge the storage system, the process is reversed so that the stored heat is transferred back from the hot molten salt to the now colder HTF. As previously mentioned, the indirect storage method offers the ability to use different fluids for the collection loop and storage system.

For a direct two-tank system, the hot and cold tanks are not connected but are installed separately in the collection loop. The hot tank is installed between the outlet of the collector field and the inlet to the power block. The corresponding cold tank is installed between the outlet of the power block and the inlet to the collection field. To charge the storage system, HTF from the collector field enters the hot tank at a higher flow rate than that at which HTF is dispatched from the hot tank to the power block, increasing the internal fluid volume. A volume of HTF located in the cold tank is simultaneously depleted to sustain the flow rate difference. To discharge the system, the system flow rates are adjusted such that the hot tank is depleted and the cold tank is filled with salt exiting the power block.

While two-tank storage systems have been demonstrated at a commercial scale, significant cost savings can be realized by combining the hot and cold HTF reservoirs into a single volume, as is done in a single-tank or thermocline energy storage system. Stable thermal stratification of the fluid region is maintained by large buoyancy forces (generated by differences in density between the hot and cold HTF) relative to mixing forces associated with the fluid

11

flow. As a result, cold HTF remains in the lower portion of the tank while hot HTF remains in the upper portion. Transitional temperatures between the hot and cold values are observed within a thin layer of large temperature gradient known as the *thermocline* or *heat-exchange region*. The vertical location of this region varies in time as the tank is charged with hot and cold HTF. Also to reduce cost, a low-cost filler material fills much of the thermocline tank volume and acts as the primary thermal storage medium. Since sensible storage occurs in both the HTF and the filler, a thermocline tank is in fact a dual-media storage system. As an unconsolidated porous medium, conduction pathways in the solid (typically a bed of rocks) are highly constricted and do not disrupt thermal stratification in the tank.

As with the two-tank design, a thermocline tank is either installed within the collection loop (direct integration) or isolated with the use of an additional heat exchanger (indirect integration). A schematic diagram of a central-receiver plant with direct integration thermocline system is provided in Figure 1 [14]. To charge the thermocline, excess hot HTF enters the top of the tank while cold HTF exits at the bottom. For discharge, the flow is reversed so that cold HTF is pumped in at the bottom while hot HTF exits at the top. The design and performance of thermocline systems are of significant current interest to CSP plants and are discussed in the next section.

As sensible heat storage increases with fluid temperature, fluids with high melting temperatures are desired to maximize the energy content and usefulness of the storage system for power generation. In early studies and applications, various oils were used as the HTF. First-generation CSP plants used Caloria HT-43, a mineral oil that could be heated to temperatures up to 315 °C. Subsequent plants (including SEGS) used different synthetic oil, Therminol VP-1, to achieve higher liquid temperatures up to 400 °C.

12

Although their use has been demonstrated in applications, these fluids suffer a number of disadvantages including high cost, flammability, and low boiling points that limit thermodynamic efficiencies in the power block. Molten salts are more viable high-temperature HTFs as they can operate at temperatures of up to 450-600 °C. In addition, molten salts are cheaper than synthetic oils, non-flammable, and non-toxic. Common commercial molten salts include Solar Salt (60% $NaNO_3$, 40% KNO_3), HITEC (53% KNO_3, 40% $NaNO_2$, 7% $NaNO_3$), and HITEC XL (48% $Ca(NO_3)_2$, 45% KNO_3, 7% $NaNO_3$). Kearney *et al.* [15] studied these different salts to determine the economic benefits of a CSP with molten-salt storage relative to existing Therminol VP-1 plants without storage. Using molten salt at a maximum temperature of 500 °C, direct two-tank storage was found to reduce the levelized electricity cost (LEC) by 17.6% while a molten-salt thermocline reduced the LEC by 20.6%.

Given the economic benefits of thermal storage, sensible energy storage systems have been installed in multiple CSP plants. The earliest storage system was a thermocline tank installed in the Solar One pilot plant from 1982 to 1986. As a central-receiver plant with direct steam generation, indirect integration of the tank was applied with Caloria HT-43 mineral oil as the thermocline HTF. With a respective diameter and height of 60 feet and 40 feet, the energy storage capacity of the thermocline tank was 170 MWh_t. Due to insufficient heliostats for excess energy collection [2], operation of the thermocline was limited to auxiliary steam generation[1].

For commercial power generation, a direct two-tank 110 MWh_t storage system was included in the SEGS I parabolic-trough plant in 1985. The Caloria oil operated between 175 °C

---

[1] While initially successful, the Solar One thermocline was permanently damaged in 1986 when water was injected into the tank on accident. The elevated temperature of the Caloria oil caused the injected water to vaporize, leading to overpressure and rupture of the tank. A small fire resulted from the rupture as volatile gases escaped and ignited upon contact with air. After repair, the thermocline remained offline while the pilot plant continued operations without storage until decommissioning in 1988.

and 295 °C [16]. Due to the low boiling point of the oil, the storage system was limited to generating saturated steam during discharge. An auxiliary fossil fuel burner was required to superheat the steam for electricity generation. The storage tanks were eventually destroyed in 1999 due to ignition of the Caloria. The plant currently operates without thermal storage.

Following the success of the Solar One project, the plant site was later renovated with additional heliostats and operated as the Solar Two plant from 1995 to 1999. The storage process was also updated with a direct two-tank design filled with molten salt, sized to support 3 hours of full load output during discharge. The use of this system proved very successful, enabling electricity generation for 153 consecutive hours in the summer of 1998 [17].

5. Thermocline Design

Significant interest in molten-salt thermocline tanks for CSP plants has resulted from the lower operational costs associated with this form of thermal storage. Extensive experimental studies of both HTF and filler material have accompanied performance modeling in order to optimize tank operation and improve storage viability.

As a dual-media system, selection of the filler material in the thermocline is important not only to minimize cost but to avoid degradation from continuous exposure to the molten salt. To determine the optimum filler, Pacheco *et al*. [16] exposed various rock materials (taconite, limestone, marble, and quartzite) to over 350 cycles of Hitec XL salt between 290 °C and 400 °C. Of the tested materials, taconite and quartzite rock were found to be the most wear resistant, with quartzite being the preferable option due to its lower cost. An experimental 2.3 MWh$_t$ thermocline tank was then constructed with quartzite rock along with silica sand to reduce the void fraction. The test module was subjected to cyclic operation as well as standby periods in

14

order to track heat losses to the surroundings. To validate the utility of the design concept, an economic analysis determined that a quartzite molten-salt thermocline tank required only two-thirds of the cost associated with an equivalent two-tank molten-salt storage system.

Until recently, few simulations of thermocline performance have been reported in the literature. Kolb [18] developed a CSP plant system model using TRNSYS commercial software to simulate the theoretical addition of a 30 MWh$_t$ thermocline tank to the 1 MW Saguaro parabolic trough plant near Tucson, AZ. The thermocline tank was modeled in TRNSYS as a one-dimensional component with thermal losses enforced at the roof and floor. The performance of the thermocline model was validated against experimental data from the Solar One thermocline tank. The resultant system simulation revealed that thermocline storage in conjunction with an expanded heliostat field increased the capacity factor of the Saguaro plant from 23% to 42%. Bharathan and Glatzmaier [19] adopted a computational fluid dynamics (CFD) approach to simulate the thermal response of a quartzite sphere in molten-salt flow. For cooling of a one-inch quartzite sphere with molten salt, the exponential decay in temperature was determined to have a time constant between 100 and 200 s.

The thermal behavior and storage efficiency of thermoclines under different operating conditions was recently analyzed by Yang and Garimella [20], who developed an axisymmetric two-temperature model of a molten-salt thermocline tank during discharge. The thermocline unit considered for analysis is schematically illustrated in Figure 2 [21]. The height of the filler region is denoted h, while h' is the height of the distributor region, d the diameter of the tank, and d' the diameter of the ports. In practice, flow distributors are generally employed to ensure a uniform flow condition at the inlet and outlet of the filler region. The characteristic length of the distributor is much larger than the particle size in the filler region. Also, the molten salt is

pumped into the distributor through the port at a velocity much larger than that in the filler region because of the small cross-sectional area of the port relative to the open frontal area of the filler region. For these two reasons, a high-Reynolds-number turbulent flow is present in the distributor region while flow in the filler region is laminar at a much lower Reynolds number.

In the filler region, the mass and momentum transport equations for the salt flow are:

$$\frac{\partial(\varepsilon\rho_l)}{\partial t} + \nabla\cdot(\rho_l\mathbf{u}) = 0 \tag{1}$$

$$\frac{\partial(\rho_l\mathbf{u})}{\partial t} + \nabla\cdot\left(\rho_l\frac{\mathbf{u}\mathbf{u}}{\varepsilon}\right) = -\varepsilon\nabla p + \nabla\cdot\tilde{\boldsymbol{\tau}} + \varepsilon\rho_l\mathbf{g} + \varepsilon\left(\frac{\mu}{K}\mathbf{u} + \frac{F}{\sqrt{K}}\rho_l|\mathbf{u}|\mathbf{u}\right) \tag{2}$$

where $\tilde{\boldsymbol{\tau}} = 2\mu\tilde{\mathbf{S}} - \frac{2}{3}\mu\mathrm{tr}(\tilde{\mathbf{S}})$ is the stress deviator tensor and $\tilde{\mathbf{S}} = \frac{1}{2}(\nabla\mathbf{u} + (\nabla\mathbf{u})^T)$ is the rate of strain tensor. In the axisymmetric coordinate system shown in Fig. 2, the problem is two-dimensional, and the velocity vector is $\mathbf{u} = u_r\mathbf{e_r} + u_x\mathbf{e_x}$ and its derivatives in the θ-direction are all zeros. In the filler region, a Reynolds number for the HTF can be defined with respect to the particle size and the kinematic viscosity at the cold inlet:

$$\mathrm{Re} = \frac{u\cdot d_s}{\nu_c} \tag{3}$$

Since the HTF and the filler material may be at different temperatures due to their distinct thermal conductivities and heat capacities, the energy equation is applied separately to the two phases. For the HTF, the energy equation is:

$$\frac{\partial[\varepsilon\rho_l C_{P,l}(T_l - T_c)]}{\partial t} + \nabla\cdot[\rho_l\mathbf{u}C_{P,l}(T_l - T_c)] = \nabla\cdot(k_e\nabla T_l) - p\nabla\cdot\mathbf{u}$$
$$+ \mathrm{tr}\left[\nabla\left(\frac{\mathbf{u}}{\varepsilon}\right)\cdot\tilde{\boldsymbol{\tau}}\right] + \frac{\mathbf{u}\cdot\mathbf{u}}{2\varepsilon}\times\frac{\partial\rho_l}{\partial t} + h_i(T_s - T_l) \tag{4}$$

Heating of the HTF as a result of compression work due to volume expansion/shrinkage, viscous effects and kinetic energy changes (respectively shown in the second, third, and fourth terms on

the right side of Eq. 4) are small and less than 10^{-4} times the conduction or convection terms, but are included for completeness.

For the filler material, the energy equation is:

$$\frac{\partial\left[(1-\varepsilon)\rho_s C_{P,s}(T_s - T_c)\right]}{\partial t} = -h_i(T_s - T_l) \tag{5}$$

The heat transfer between the HTF and the filler is accounted for with a volumetric interstitial heat transfer coefficient h_i, which appears as a source term on the right side of both Eq. 4 and 5. Energy losses from the tank to the surroundings are neglected in this analysis, but are considered later in this discussion.

As an unconsolidated porous medium, the filler particles are completely surrounded by the HTF and exhibit poor thermal contact with neighboring particles. Treating the filler as a dispersed phase embedded in a continuous HTF, effective thermal conductivity of the dual-media mixture in Eq. 4 can then be expressed as [22]:

$$k_e = k_l \frac{1 + 2\beta\phi + (2\beta^3 - 0.1\beta)\phi^2 + \phi^3 0.05\exp(4.5\beta)}{1 - \beta\phi} \tag{6}$$

where $\phi = 1 - \varepsilon$ and $\beta = (k_s - k_l)/(k_s + 2k_l)$. Eq. 6 provides a good estimate for the effective conductivity of liquid-saturated porous media with φ ranging from 0.15 to 0.85 and β from -0.499 to 1. In the filler phase, thermal conduction is neglected because of large thermal contact resistance between filler particles. Conduction is also neglected within the particles due to their small size; thus, temperature changes in the filler particles are thus solely due to heat exchange with the HTF phase.

Representative simulations are conducted with HITEC molten salt as the HTF and quartzite rock as the filler material. The physical properties of HITEC change with temperature and are calculated according to the following curve fits to experimental measurements [23]:

17

$$\rho_l = 1938.0 - 0.732(T_l - 200.0) \tag{7}$$

$$\mu = \exp\left[-4.343 - 2.0143(\ln T_l - 5.011)\right] \tag{8}$$

$$k_l = -6.53 \times 10^{-4}(T_l - 260.0) + 0.421 \tag{9}$$

The fits in Eqs. 7-9 represent the experimental data with maximum errors of 0.2%, 0.5%, and 0.8%, respectively. The heat capacity of the HITEC is relatively constant at 1561.7 J/kg-K according to published data. Properties of quartzite rock are treated as constants, with a specific heat capacity and density of 830 J/kg-K and 2500 kg/m^3, respectively [24].

5.1   Numerical Simulation

The governing transport equations are solved using the finite volume method with the commercial software package, FLUENT [25]. The computational domain is discretized into finite volumes. All the variables are stored at the centers of the square mesh cells. A second-order upwind scheme is used for the convective fluxes, while a central-differencing scheme is used for the discretized diffusion fluxes. A second-order implicit scheme is used for the time discretization. Pressure-velocity coupling is implemented through the PISO algorithm [26]. Iterations at each time step are terminated when the dimensionless residuals for all equations drop below 10^{-4}.

To simulate flow in the distributors, the standard k-ε model with a standard wall function is employed [27]. According to Wakao and Kaguei [9], the interstitial Nusselt number for liquid flow through particles beds can be expressed as:

$$\mathrm{Nu}_i = 6(1-\varepsilon)\left[2 + 1.1\,\mathrm{Re}_L^{0.6}\,\mathrm{Pr}_L^{1/3}\right] \tag{10}$$

where Re_L and Pr_L are the local Reynolds and Prandtl numbers, respectively.

Assuming the distributor regions are properly designed so that uniform flow at the inlet and outlet of the filler region has been achieved, the appropriate boundary conditions are as follows.

At the inlet:

$$u_x = u_m, \ u_r = 0, \ T_l = T_c \tag{11}$$

At the outlet:

$$\frac{\partial u_x}{\partial x} = \frac{\partial u_r}{\partial x} = \frac{\partial T_i}{\partial x} \tag{12}$$

Experimental results from the test module discussed in [16] are used to validate the numerical model [20].

5.2   Numerical Results

Once validated, the code is employed to systematically investigate the discharge characteristics of a thermocline energy storage unit. For comparing the performance of different thermocline setups, it is useful to non-dimensionalize the tank height with respect to particle size, as well as the temperatures with respect to the operating limits:

$$H = \frac{h}{d_s} \tag{13}$$

$$\Theta_l = \frac{T_l - T_c}{T_h - T_c} \tag{14}$$

$$\Theta_s = \frac{T_s - T_c}{T_h - T_c} \tag{15}$$

During discharge, it is convenient to track the location where molten salt is at the middle temperature ($\Theta_l = 0.5$) as representative of the heat exchange zone, denoted with the non-dimensional height, X_m. Translation of the heat exchange zone is thus recorded in a moving

19

coordinate system with X_m as the origin. Both the filler and molten-salt temperature profiles are nearly symmetric around this origin; thus, the overall energy transport from the moving control volume is assumed to be zero to a good approximation. As such, the speed of the heat exchange region in the thermocline during discharge can be deduced from a simple energy balance:

$$v = \frac{Cp_{l,c}\rho_{l,c}u_m}{\varepsilon Cp_{l,c}\rho_{l,c} + (1-\varepsilon)Cp_s\rho_s} \qquad (16)$$

Figure 3 shows the development of the axial temperature profiles plotted in the moving coordinate system for Re = 1 and Re = 10, with the horizontal axis being $(X - X_m)$. All the temperature profiles pass through the point (0, 0.5) and appear to be symmetrical about this point as mentioned above. As the discharge process proceeds (and the height of the heat-exchange zone X_m increases), the thermal energy decrease (temperature drop) in the region to the right of the point (0, 0.5) is effectively compensated by an increase (temperature rise) in the region to the left of the point.

Increasing the Reynolds number results in an expansion of the heat-exchange zone. For instance, the temperature profiles at Re = 10 change more gradually in the heat-exchange zone than at Re = 1 when compared at the same position X_m, resulting in a wider heat-exchange zone, as shown in Fig. 3. At the higher Reynolds number, a longer flow distance is needed for the fluid to be heated by the filler phase, leading to a more gradual temperature rise and a corresponding increase in the extent of the heat-exchange zone. Since the molten salt in the heat-exchange zone is at a relatively lower temperature, expansion can lead to significant waste of thermal energy if the salt delivered at lower temperatures is not useful for further application.

Prior to the heat-exchange zone reaching the tank outlet, salt at a constant high-temperature level ($\Theta_l = 1$) is available at the outlet. As the heat-exchange zone arrives at the outlet, the salt temperature begins to drop, finally reaching the constant low temperature level (Θ_l

20

= 0) when thermal energy stored in the filler particles has been completely depleted. Thermocline tanks with a larger height can effectively extend the discharge state wherein the salt temperature is maintained at a high level. Since the low-temperature salt is not acceptable for generating superheated steam in the turbines, it is desired that most of the stored thermal energy be retrieved at a high-temperature level in order to meet design conditions and maintain reasonable thermal-to-electrical conversion efficiency in the turbine generator.

To compare various thermocline designs, it is of interest to quantify the amount of useful energy that a thermocline system can deliver during a discharge cycle. The discharge efficiency for thermocline thermal energy storage may be defined as follows:

$$\eta = \frac{Output\ energy\ with\ \Theta_l > \Theta_0}{Total\ initial\ energy\ stored\ in\ the\ thermocline} \qquad (17)$$

where Θ_0 is a threshold value determined by the application of interest. A relatively stringent value of 0.95 for Θ_0 is chosen for analysis, implying that thermal energy values delivered at temperatures greater than $(T_c + 0.95(T_h - T_c))$ qualify as useful energy. The efficiency defined by Eq. 17 varies depending on the construction and working conditions of the thermocline system. Figure 4 shows the discharge efficiency calculated for different Re for thermoclines of different heights H. It is clear that the efficiency increases with tank height H, and decreases with a rise in the Reynolds number. The numerical results for the efficiency in Fig. 4 are well represented by the following correlation:

$$\eta = 1 - 0.1807\,\mathrm{Re}^{0.1801}\left(H/100\right)^m \qquad (18)$$

where $m = 0.00234\mathrm{Re}^{-0.6151} + 0.00055\mathrm{Re} - 0.485$. This correlation can predict the numerical data with maximum error of 1% for Reynolds number between 1 and 50 and H between 10 and 800,

as shown by the predictions from the equation included in Fig. 4. It is emphasized, however, that this correlation represents results for the chosen value of 0.95 for Θ_0.

Three other important parameters which capture the performance of the thermocline system, *i.e.*, discharge power per unit cross-sectional area (*P/A*), useful thermal energy per unit cross-sectional area (*Q/A*), and total stored thermal energy per unit cross-sectional area (*Q_t/A*), may be defined as follows:

$$\frac{P}{A} = u_m \rho_{l,c} C p_{l,c} \left(T_h - T_c \right) = k_{l,c} \frac{T_h - T_c}{d_s} \operatorname{Re} \operatorname{Pr} \tag{19}$$

$$\frac{Q}{A} = \left[\varepsilon \rho_{l,h} C p_{l,h} + \left(1 - \varepsilon \right) \rho_s C_{Ps} \right] \left(T_h - T_c \right) \cdot d_s \cdot H \eta \tag{20}$$

$$\frac{Q_t}{A} = \left[\varepsilon \rho_{l,h} C p_{l,h} + \left(1 - \varepsilon \right) \rho_s C_{Ps} \right] \left(T_h - T_c \right) \cdot d_s \cdot H \tag{21}$$

where Q is the useful thermal energy delivered (at a temperature above Θ_0). From the above equations, a non-dimensional discharge power may be defined as RePr, a non-dimensional useful energy as $H\eta$, and a non-dimensional total energy as *H* (equaling the non-dimensional tank height). Using these designations, Figure 5 plots the efficiency for various values of discharge power and total energy. The discharge efficiency increases with an increase in the stored thermal energy and decreases with an increase in discharge power. Thus a high-efficiency tank should have a large height (within practical limits) and operate at a low discharge power. According to a recent design study by the Electric Power Research Institute [14], thermocline tanks should not exceed 39 feet (11.9 m) in order to avoid excessive load on the foundation.

5.3   Design Procedure

A design procedure for thermocline tanks with HITEC molten salt and quartzite filler is developed based on the computations discussed above. It is assumed that useful thermal energy

Q and discharge power P are known *a priori* for the storage application. The recommended procedure [20] is as follows:

1. Choose tank diameter d and filler particle size d_s based on practical requirements.

2. Calculate the cross-sectional area of the storage tank, and then the discharge power per unit cross-sectional area (P/A) and useful thermal energy per unit cross-sectional area (Q/A).

3. Calculate the non-dimensional discharge power RePr and useful thermal energy $H\eta$ using Eqs. 19 and 20, respectively.

4. Calculate Re from the value of RePr and assume $H = H\eta$.

5. Use Re and H values to calculate η from Eq. 18.

6. Obtain H by dividing $H\eta$ with η obtained in step 5.

7. Repeat steps 5 and 6 until convergence of H within 0.1%.

8. The final η and H are the discharge efficiency and required height for the thermocline tank.

9. The dimensional tank height is calculated as $h = d_s \cdot H$.

Table 1 shows some examples of thermocline designs based on this procedure for a storage tank initially at 450 °C with cold HITEC at 250 °C fed into the bottom of the tank. Thermal energy delivered at a temperature exceeding 440 °C ($\Theta_0 = 0.95$) is regarded as useful energy in these examples.

6. Thermocline Performance

While the methodology discussed in the previous section allows for a detailed analysis of the design and operation of an ideal thermocline, the performance of tanks in practice may be

significantly affected by additional mechanisms including external heat losses as well as thermomechanical stresses that build up in the tank wall. These mechanisms are discussed in this section.

6.1   External Losses

To investigate the effects of thermal losses to the surroundings, Yang and Garimella [21] extended the discharge model to include non-adiabatic tank wall conditions. In addition to the governing equations and boundary conditions described earlier, these losses are enforced along the tank wall (in non-dimensional form) as:

$$\frac{\partial \Theta_l}{\partial n} = \alpha_k \, \mathrm{Nu}_w \left(\Theta_w - \Theta_\infty \right) \tag{22}$$

where $\mathrm{Nu}_w = h_{conv} d / k_{air}$, and α_k is the ratio of the thermal conductivity of the surrounding air (0.0242 W/m-K) to the effective thermal conductivity of molten salt in turbulent flow (at the distributor walls) or laminar flow (at the filler bed walls); n is the directional unit normal to the wall and points into the tank. The parameter h_{conv} is an effective heat transfer coefficient, which is expressed as $h_{conv} = q^{''} / \left(T_w - T_\infty \right)$, where T_0 is the surrounding air temperature and T_w is the molten-salt temperature at the tank wall. The conductive resistance of tank wall is included in h_{conv}.

Typical flow streamlines and temperature distributions at different stages during the discharge process of the thermocline tank are presented in Figure 6 for an adiabatic wall and in Figure 7 for a non-adiabatic wall with $\mathrm{Nu}_w = 1.6 \times 10^5$. The non-dimensional time associated with the stages is defined as:

$$\tau = \frac{t \cdot u_m}{h} \tag{23}$$

When the tank wall is adiabatic, no heat exchange takes place between the molten salt inside the tank and the surrounding air outside the tank. The flow streamlines are then straight and uniform in the filler bed (the region from 0 to 1 in the vertical direction) due to the presence of effective distributors at the top and bottom of the filler bed. Thermal stratification is well established in the filler bed for this adiabatic-wall case.

When the tank wall is non-adiabatic, flow streamlines are no longer straight lines in the filler bed: instead, a recirculation pattern is formed in the top-left corner of the filler bed, as shown in Fig. 7. The wall Nusselt number chosen here represents a wall exposed to an effective heat transfer coefficient h_{conv} = 100 W/m²-K for a tank of diameter 40 m and surrounding air temperature of 25 °C (Θ_0 = -1.125, for T_{h} = 450 °C and T_{c}= 250 °C). The recirculation cell in the top-left corner of the filler bed is formed by a downward flow adjacent to the wall, where the molten salt is cooled by the outside air and becomes heavier. As the discharge process proceeds, the cell shrinks and finally vanishes (as seen in the change in flow field from τ = 0.069 to 0.69 in Fig. 6) due to the approach of the cooler flows from the bottom and from the side wall. A cooler region (Θ_{l} < 0) is also seen to grow in the bottom-left corner of the tank (τ = 0.33 and 0.69), as a direct consequence of interaction with cooling at the wall. The non-adiabatic wall also causes the high-temperature zone in Fig. 7 to shrink faster than it does in Fig. 6.

To fully inspect the discharge behavior, it is instructive to examine the temperature of molten-salt outflow from the top port of the thermocline. Figure 8 shows the temperature histories under adiabatic and non-adiabatic tank wall conditions for different Reynolds numbers. In general, all profiles maintain a high temperature level for some initial part of the discharge process and then drop rapidly in value. In an adiabatic-wall thermocline, the temperature of the outflow is maintained at a constant high level for much of the discharge process, dropping only

when the heat-exchange zone approaches the top port. As previously noted, larger Reynolds numbers increase the extent of the heat exchange zone and lead to a temperature drop at earlier times.

In a thermocline with a non-adiabatic wall, the high-temperature period of outflow is no longer held at a constant level. The gradual decrease early in the discharge is caused by the heat loss at the tank wall, while the rapid decrease later is again due to the arrival of the heat-exchange zone at the top port. Temperature fluctuations within the discharge process may be attributed to recirculation cells of cold molten salt exiting the top port which are caused by the heat loss at the top wall of the thermocline. The influence of Reynolds number in non-adiabatic thermoclines shows an opposing trend to the previous adiabatic data. Since the molten-salt flow rate decreases with decreasing Reynolds number, the discharge time (dimensional) increases, in turn increasing the energy loss at the tank wall and causing a general drop in temperature. This not only decreases the outflow temperature but also causes a more rapid decrease in the outflow temperature at small Reynolds numbers. On the contrary, increasing the Reynolds number shortens the (dimensional) discharge time and minimizes the influence of heat loss at the tank wall, which renders the outflow history to be more similar to that for an adiabatic thermocline.

Figure 9 shows the discharge efficiency for thermoclines with different environmental boundary conditions with respect to the heat loss at the tank wall. It is interesting to note that for a modest wall Nusselt number such as $Nu_w = 1.6 \times 10^4$, the discharge efficiency first increases and then decreases as the Reynolds number increases. The initial increase indicates that the increased discharge time (dimensional) has a dominant influence on the discharge efficiency, while the subsequent decrease shows that the expansion of the heat-exchange zone caused by the increase in Reynolds number has a more important effect on the efficiency. As the Reynolds

26

number increases to Re = 250 in Fig. 9, the discharge time is severely reduced, which minimizes the effects of the heat loss on the tank wall and causes the values of efficiency at the two non-adiabatic boundaries to approach those for an adiabatic thermocline.

6.2   Thermal Ratcheting

An operating thermocline system goes through repeated discharge and charge cycles. The effect of cyclic operation is temperature oscillation throughout the fillerbed and tank wall of the thermocline. While unavoidable, care must be taken to ensure that these oscillations do not lead to a failure mode known as thermal ratcheting.

Thermal ratcheting is a process by which the tank wall of the thermocline is progressively expanded from cyclic operation leading to catastrophic failure of the wall material. If the thermal expansion coefficient of the tank wall is greater than that of the filler particles, a radial gap develops between the two materials whenever the tank is heated. The fillerbed reorients (slumps) to fill this gap. When the tank is then cooled, the wall cannot contract to its original diameter and generates a hoop stress proportional to the strain of the initial expansion. If this stress exceeds the yield strength of the wall material, plastic deformation occurs and the wall effectively *ratchets* to a new diameter. As such ratcheting motions accumulate, the hoop stress increases until the ultimate strength of the material is exceeded, causing the tank to rupture. If on the other hand, this stress does not exceed the yield strength, the original thermal strain is fully recovered in the next heating process and the tank does not experience additional ratcheting. An investigation of thermal ratcheting was conducted for the Solar One mineral oil thermocline, but it was determined to be an improbable failure mode as the filler particles experienced greater thermal expansion than the tank wall in this case [28].

To avoid thermal ratcheting, temperature oscillations in the tank wall must be minimized in order to reduce the stress-strain interactions associated with cyclic operation of the thermocline. This is achieved through the inclusion of insulation layers in the thermocline design. However, some amount of oscillation will occur in the tank wall regardless of the extent of insulation applied. Therefore the wall should be composed of material with high resiliency to accommodate the stress.

To investigate the ratcheting phenomenon, Flueckiger *et al*. [29] extended the CFD simulation from [21] to include a composite wall composed of internal insulation ($k = 1$ W/m-K, $\rho = 2000$ kg/m^3, $C_P = 1000$ J/kg-K), steel shell ($k = 60$ W/m-K, $\rho = 8000$ kg/m^3, $C_P = 430$ J/kg-K), and external insulation ($k = 1$ W/m-K, $\rho = 1000$ kg/m^3, $C_P = 1000$ J/kg-K). The assigned thermal transport properties for these layers correlate to common engineering values for steel and insulation materials. In reality, a thin liner material also surrounds the filler material to protect the internal insulation, but its effect is assumed to be negligible in this analysis. For mechanical analysis of the steel, the coefficient of thermal expansion, modulus of elasticity, and yield strength are assigned to take typical values of 0.00001 K^{-1}, 200 GPa, and 200 MPa, respectively. To model the stress along the thermocline tank, the internal filler is assumed to be cohesionless (no resistance to slumping) and infinitely rigid (immune to mechanical deformation). The result is a conservative approximation in which stress is proportional to the magnitude of temperature fluctuations inside the steel shell.

The thermocline tank was subjected to seven different scenarios, as listed in Table 2. Cases 1-4 varied the external boundary conditions along the tank surface while cases 5-7 varied the dimensions of the individual layers of the composite wall. After each case arrived at periodic behavior from cyclic charging and discharging, temperature profiles along the steel shell were

extracted and converted to hoop stresses proportional to the maximum thermal fluctuation at each discretized location. The results of these simulations are plotted in Figure 10. Stress values are normalized (ω) with respect to the yield strength of the steel shell. The maximum normalized stress values for each case are listed in Table 2. In cases 1 through 4, the maximum hoop stress is inversely proportional to the heat loss at the tank surface. Case 3 experiences the least amount of external heat transfer but records the highest peak stress value. This behavior is due to the sensitivity of the temperature distribution in the composite wall to both external losses and cyclic tank operation. Greater losses at the surface reduce sensitivity to the internal molten salt fluctuations and dampen cyclic temperature variations along the steel shell. It is also noted that all cases yield normalized peak stress values less than unity, with cases 1 through 4 clustered between 0.407 and 0.425. Thus plastic deformation-associated ratcheting would not occur in any of these cases. Since thermal ratcheting is not an issue, case 3 is preferable among the four different external boundary conditions due to the minimal energy losses to the surroundings.

Even though the tank wall does not reach high stress levels in cases 1 through 4, further reductions in stress can maximize the factor of safety associated with thermal ratcheting in the event of unexpected increases in heat loss or other unforeseen circumstances. The structure of the composite wall is modified in cases 5 through 7 in terms of the relative thicknesses of the internal insulation, steel shell, and exterior insulation layers, while the surface heat loss conditions are held at the values in case 1. Case 5 experiences the lowest overall peak stress in the steel shell, with a normalized value of 0.129 due to the increased internal insulation thickness. The added insulation between the filler region and the steel in this case diminishes sensitivity to the fluctuating molten-salt temperatures. Case 6 also exhibits much lower stress

29

levels, with a normalized value of 0.333. The thicker steel layer in this case increases axial conduction which reduces temperature gradients along the shell.

In contrast to the behavior of the internal insulation and steel layers, the external insulation thickness must be reduced to decrease hoop stress in the steel shell. Thinner insulation increases the sensitivity of the steel shell to the external losses, which in turn decreases sensitivity to the cyclic molten-salt behavior and dampens temperature fluctuations. This effect is seen in case 7, where the external insulation thickness is reduced by half compared to the other cases to yield a peak normalized hoop stress of 0.391. However since the peak stress is only reduced by 5% compared to case 1, a larger external layer remains preferable to maximize total insulation between the filler region and the surroundings.

In the event of a tank shutdown or startup, the magnitude of temperature oscillations along the tank wall increase dramatically. As a result, the infinite rigidity approximation associated is no longer valid as thermally-induced volume changes in the granules become non-negligible. To simulate such conditions, inclusion of a detailed model of the granular physics inside the tank becomes necessary.

7. Closure

Renewed interest in thermal energy storage for concentrating solar power plants has led to a significant growth in both the understanding and capability of thermal storage technologies. These technologies include a diverse array of different storage mechanisms, materials, and system integration approaches. Of these, molten-salt thermocline tanks have the potential to provide storage capability without incurring excessive cost. Based on multiple numerical investigations, discharge performance of a thermocline has been shown to be strongly dependent

on the tank height as well as the molten salt flow rate, expressed as a Reynolds number. A design procedure is developed to assess the discharge performance of thermocline tanks containing molten salt and rock beds. Large tank heights increase the storage capacity of the thermocline and delay the arrival of the heat exchange region at the outlet port. For an adiabatic wall condition, low Reynolds number flows in the thermocline reduce the extent of the heat-exchange zone, lower the entropy generation associated with the heat exchange between the molten salt and filler, and thus improve the overall discharge efficiency. However for highly non-adiabatic conditions, a low Reynolds number is detrimental to discharge performance as the increased residence time of the molten salt in the tank is subject to a greater amount of heat loss to the surroundings. Potential tank failure through thermal ratcheting is mitigated by the inclusion of internal insulation and the use of highly resilient steel for the tank wall.

Despite its limited incorporation in existing CSP plants, continued investigation of thermal energy storage will further the viability and performance of these systems. While much of this work has focused on material studies and simulation, there is now a need for experimental investigations at different scales (laboratory to pilot plant to commercial) in order to increase real world data and operational experience. Such studies can help in developing thermal storage into a low cost and reliable addition to power plants.

Nomenclature

C_P specific heat, J/kg-K

d diameter of thermocline tank, m

d' diameter of inlet and outlet ports, m

d_s diameter of filler particles, m

$\mathbf{e}_r$ unit vector in the r direction, -

$\mathbf{e}_x$ unit vector in the x direction, -

F inertial coefficient, $F = \dfrac{1.75}{\sqrt{150\varepsilon^3}}$ [8],-

g gravity, m/s^2

h height of thermocline, m

h' height of distributor region, m

h_i interstitial heat transfer coefficient, W/m^3-K

h_{conv} wall heat transfer coefficient, W/m^2-K

K permeability, $K = \dfrac{d_s^{\,2}\varepsilon^3}{175(1-\varepsilon)^2}$ [30], m^2

k thermal conductivity, W/m-K

p pressure, Pa

T temperature, K

t time, s

$\mathbf{u}$ velocity vector, m/s

u_m mean velocity magnitude at inlet to fillerbed, m/s

u_{mag} velocity magnitude, m/s

Greek

δ   composite wall layer thickness, cm

ε   porosity, -

ε_{rad} emissivity, -

μ   viscosity, Pa-s

ν   kinematic viscosity, m^2/s

ρ   density, kg/m^3

$\tilde{\tau}$ stress tensor, N/m^2

ω   normalized stress, -

Subscript

1   internal insulation

2   steel shell

3   external insulation

c   at the inlet low temperature

h   at the outlet high temperature

l   molten salt phase

s   solid filler phase

w   at the wall

∞   at the surroundings

References

[1] Müller-Steinhagen, H., From Megawatt to Gigawatt: New Developments in Concentrating Solar Thermal Power, *Proc. International Heat Transfer Conf.*, Washington DC, 2010.

[2] Radosevich, L. G., Final Report on the Power Production Phase of the 10 MW_e Solar Thermal Central Receiver Pilot Plant, Sandia Rept. SAND87-8022, 1988.

[3] Mills, D. R., and Morrison, G. L., Compact Linear Fresnel Reflector Solar Thermal Powerplants, *Solar Energy*, vol. 68, pp. 263-283, 2000.

[4] Mills, D. R., Advances in Solar Thermal Electricity Technology, *Solar Energy*, vol. 76, pp. 19-31, 2004.

[5] Herrmann, U., and Kearney, D. W., Survey of Thermal Energy Storage for Parabolic Trough Power Plants, *Journal of Solar Energy Engineering*, vol. 124, pp. 145-152, 2002.

[6] Lovegrove, K., Luzzi, A., Soldiani, I., and Kreetz, H., Developing Ammonia Based Thermochemical Energy Storage for Dish Power Plants, *Solar Energy*, vol. 76, pp. 331-337, 2004.

[7] Felix Regin, A., Solanki, S. C., and Saini, J. S., An Analysis of a Packed Bed Latent Heat Thermal Energy Storage System Using PCM Capsules: Numerical Investigation, *Renewable Energy*, vol. 34, pp. 1765-1773, 2009.

[8] Krishnan, S., Murthy, J. Y., and Garimella, S. V., A Two-Temperature Model for Solid-Liquid Phase Change in Metal Foams, *Journal of Heat Transfer*, vol. 127, pp. 995-1004, 2005.

[9] Wakao, N., and Kaguei, S., *Heat and Mass Transfer in Packed Beds*. Gordon and Beach, New York, 1982.

[10] Yang, Z., and Garimella, S. V., Melting of Phase Change Materials with Volume Change in Metal Foams, *Journal of Heat Transfer*, vol. 132, pp. 062301 1-11, 2010.

[11] Laing, D., Bauer, T., Lehmann, D., and Bahl, C., Development of a Thermal Energy Storage System for Parabolic Trough Power Plants with Direct Steam Generation, *Journal of Solar Energy Engineering*, vol. 132, pp. 021011 1-8, 2010.

[12] Laing, D., Steinmann, W., Fiβ, M., Tamme, R., Brand, T., and Bahl, C., Solid Media Thermal Storage Development and Analysis of Modular Storage Operation Concepts for Parabolic Trough Power Plants, *Journal of Solar Energy Engineering*, vol. 130, pp. 011006 1-5, 2008.

[13] Laing, D., Lehmann, D., Fiβ, M., and Bahl, C., Test Results of Concrete Thermal Energy Storage for Parabolic Trough Power Plants, *Journal of Solar Energy Engineering*, vol. 131, pp. 041007 1-6, 2009.

[14] Solar Thermal Storage Systems: Preliminary Design Study, EPRI Rept. 1019581, 2010.

[15] Kearney, D., Herrmann, U., Nava, P., Kelly, B., Mahoney, R., Pacheco, J., Cable, R., Potrovitza, N., Blake, D., and Price, H., Assessment of a Molten Salt Heat Transfer Fluid in a Parabolic Trough Solar Field, *Journal of Solar Energy Engineering*, vol. 125, pp. 170-176, 2003.

[16] Pacheco, J. E., Showalter, S. K., and Kolb, W. J., Thermocline Thermal Storage System for Parabolic Trough Plants, *Journal of Solar Energy Engineering*, vol. 124, pp. 153-159, 2002.

[17] Solar Two Central Receiver Consultant Report, Public Interest Energy Research, P600-00-017, 1999.

[18] Kolb, G. J., Performance analysis of thermocline energy storage proposed for the 1 MW Saguaro solar trough plant, *Proc. of International Solar Energy Conf.*, Denver, CO, 2006.

[19] Bharathan, D., and Glatzmaier, G. C., Progress in Thermal Energy Storage Modeling, *Proc. of Energy Sustainability Conf.*, San Francisco, CA, 2009.

[20] Yang, Z., and Garimella, S. V., Thermal Analysis of Solar Thermal Energy Storage in a Molten-Salt Thermocline, *Solar Energy*, vol. 84, pp. 974-985, 2010.

[21] Yang, Z., and Garimella, S. V., Molten-Salt Thermal Energy Storage in Thermoclines Under Different Environmental Boundary Conditions, *Applied Energy*, vol. 87, pp. 3322-3329, 2010.

[22] Gonzo, E. E., Estimating Correlations for the Effective Thermal Conductivity of Granular Materials, *Chemical Engineering Journal*, vol. 90, pp. 299-302, 2002.

[23] HITEC Heat Transfer Salt, Coastal Chemical Co., LLC, Brenntag Company, http://www.coastelchem.com, last accessed August 2010.

[24] Specific Heat Capacities of Some Common Substances. The Engineering ToolBox, http://www.EngineeringToolBox.com, last accessed August 2010.

[25] FLUENT Documentation, Version 12.1 Users Guide, 2009.

[26] Issa, R. I., Solution of Implicitly Discretized Fluid Flow Equations by Operator Splitting, *Journal of Computation Physics*, vol. 62, pp. 40-65, 1986.

[27] Launder, B. E., and Spalding, D. B., *Lectures in Mathematical Models of Turbulence*, Academic Press, London, 1972.

[28] Faas, S. A., Thorne, L. R., Fuchs, E. A., and Gilbertsen, N. D., 10 MW$_e$ Solar Thermal Central Receiver Pilot Plant: Thermal Storage Subsystem Evaluation – Final Report, Sandia Rept. SAND86-8212, 1986.

[29] Flueckiger, S., Yang, Z., and Garimella, S. V., An Integrated Thermal and Mechanical Investigation of Molten-Salt Thermocline Energy Storage, *Applied Energy*, vol. 88, pp. 2098-2105, 2011.

[30] Beckermann, C., and Viskanta, R., Natural Convection Solid/Liquid Phase Change in Porous Media, *International Journal of Heat and Mass Transfer*, vol. 31, pp. 35-46, 1988.

Table 1: Results for various thermocline design examples

Case No.	Q (MWh)	P (MW)	d (m)	d_s (m)	η (%)	h (m)
1	5	1	2	0.05	83.6	15.2
2	5	1	2	0.1	75.4	16.8
3	5	1	5	0.05	73.4	2.77
4	5	1	5	0.1	61.4	3.31
5	5	2	2	0.05	81.6	15.6
6	5	2	2	0.1	72.4	17.5
7	5	2	5	0.05	70.5	2.88
8	5	2	5	0.1	57.6	3.52
9	10	1	2	0.05	88.0	28.8
10	10	1	2	0.1	81.6	31.1
11	10	1	5	0.05	80.1	5.07
12	10	1	5	0.1	70.5	5.76
13	10	2	2	0.05	86.4	29.4
14	10	2	2	0.1	79.1	32.1
15	10	2	5	0.05	77.8	5.22
16	10	2	5	0.1	67.3	6.03

Table 2: Summary of the cases considered with different structural wall parameters and heat loss conditions.

Case	h (W/m^2-K)	ε_{rad}	δ_1 (cm)	δ_2 (cm)	δ_3 (cm)	ω_{max}
1	5	1	10	2	5	0.412
2	10	1	10	2	5	0.407
3	5	0.5	10	2	5	0.425
4	10	0.5	10	2	5	0.416
5	5	1	20	2	5	0.129
6	5	1	10	4	5	0.333
7	5	1	10	2	2.5	0.391

List of Figures

Figure 1 Schematic diagram of a CSP plant with direct thermocline tank storage (reproduced

from [14]).
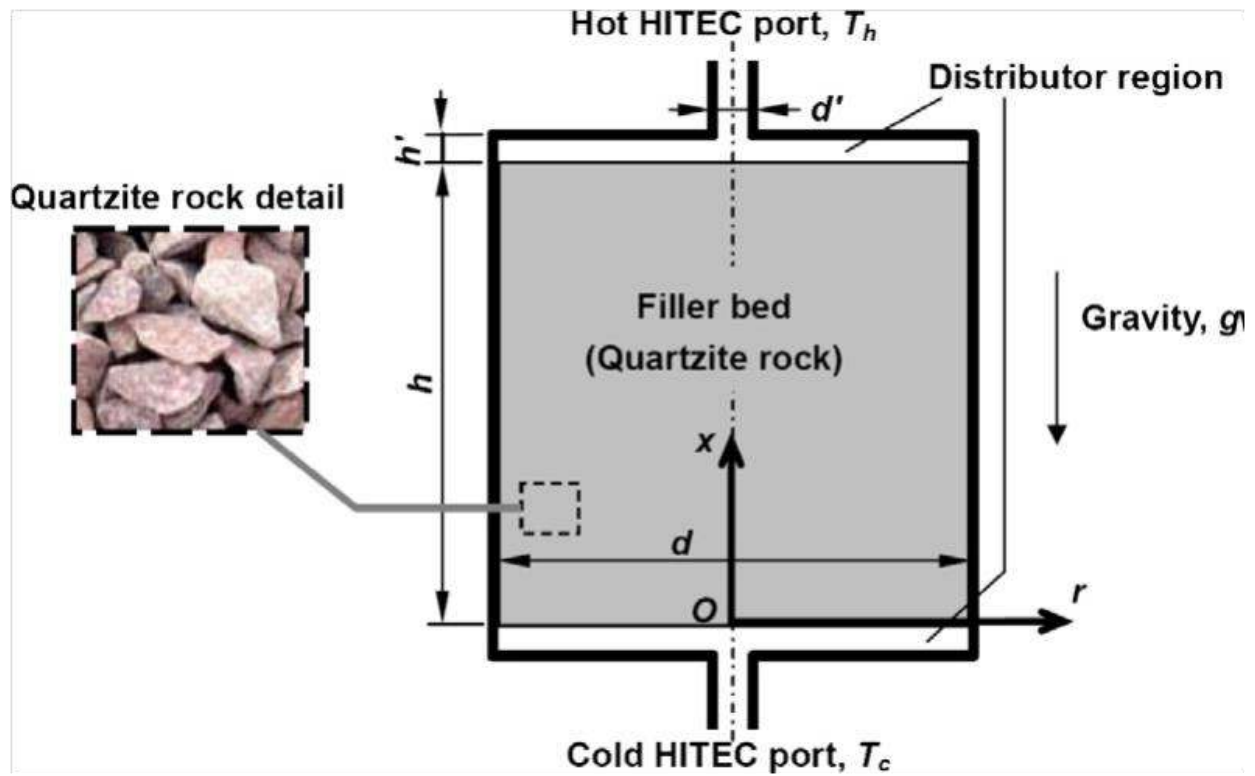
Figure 2 Schematic diagram of the thermocline thermal energy storage system under analysis

and the axisymmetric coordinate system used.
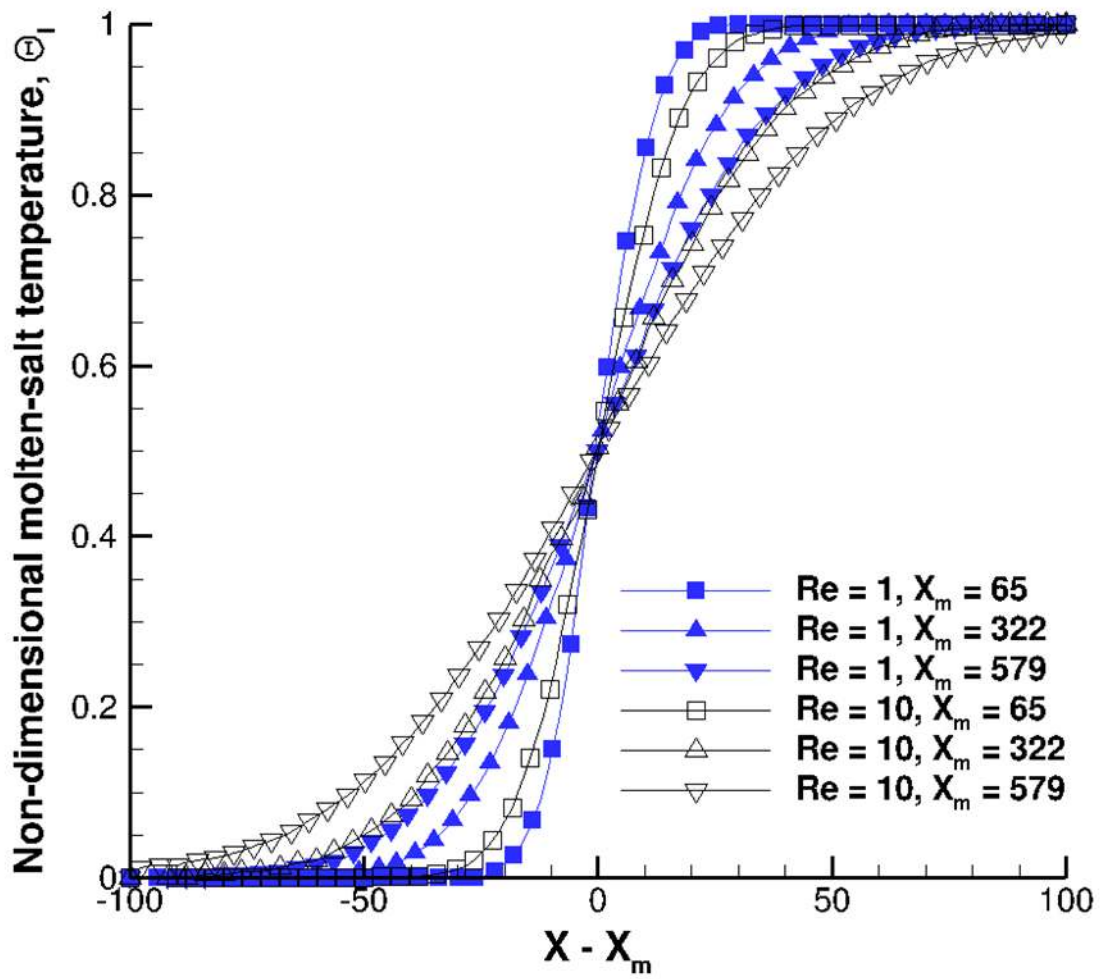
Figure 3 Development of molten salt temperature profiles in the heat-exchange zone.
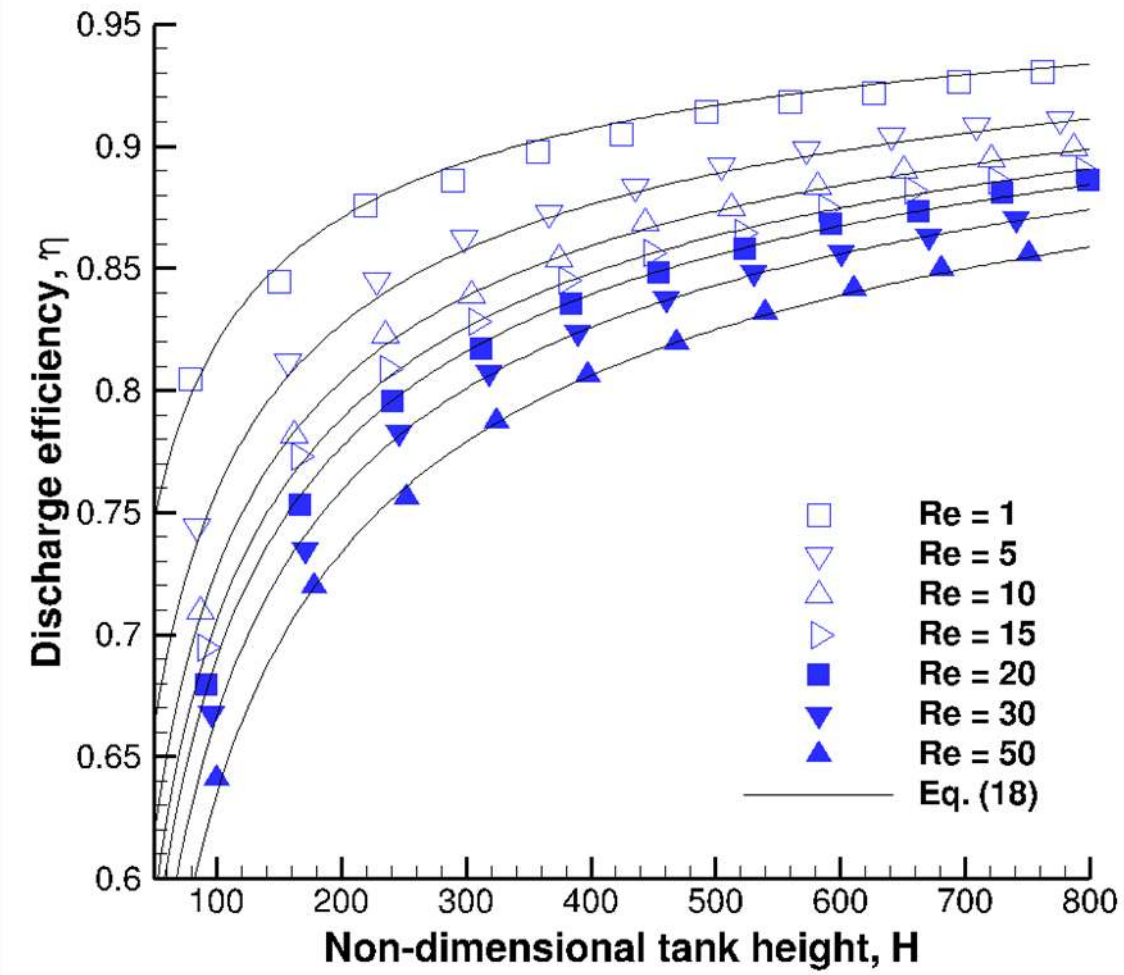
Figure 4 Discharge efficiency η of a thermocline at different *H* and Re.
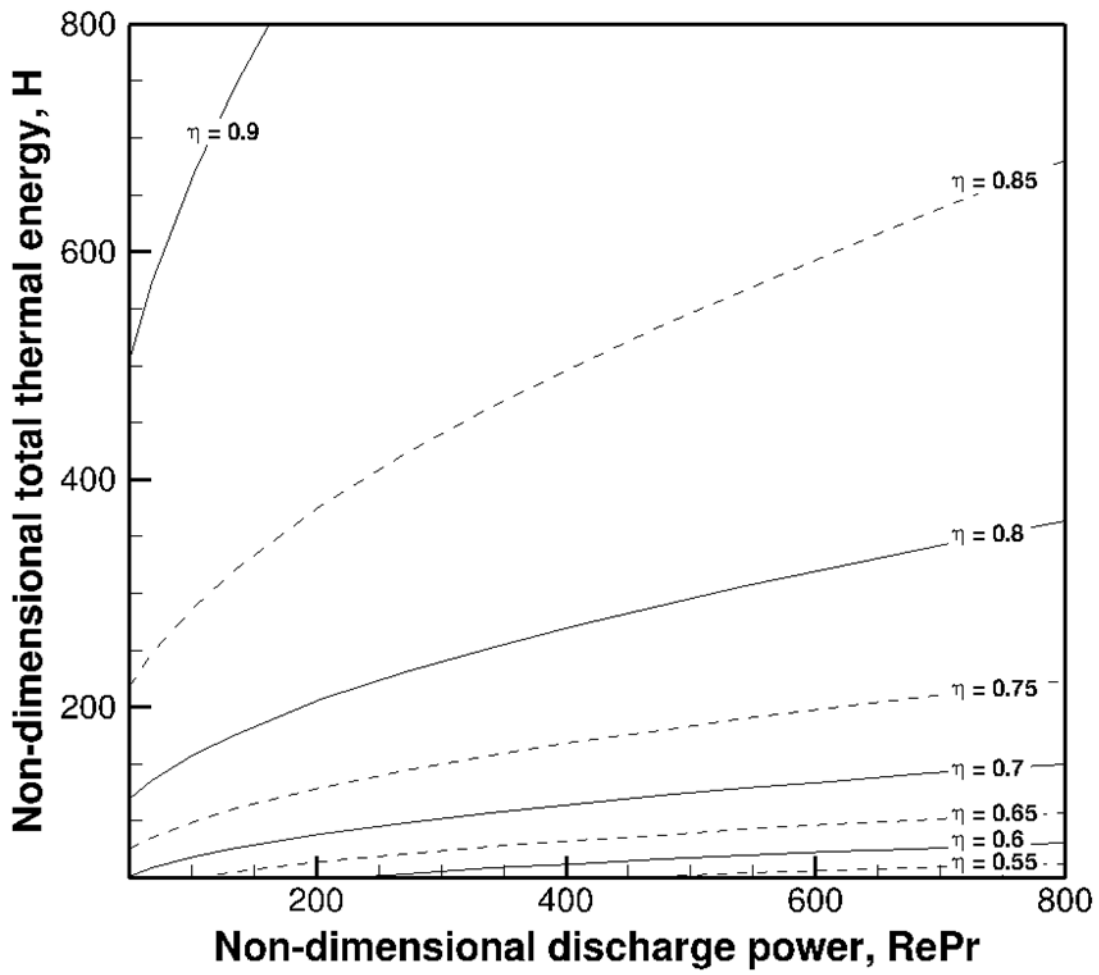
Figure 5 Discharge efficiency at different discharge powers (RePr) and total thermal energies *H*.
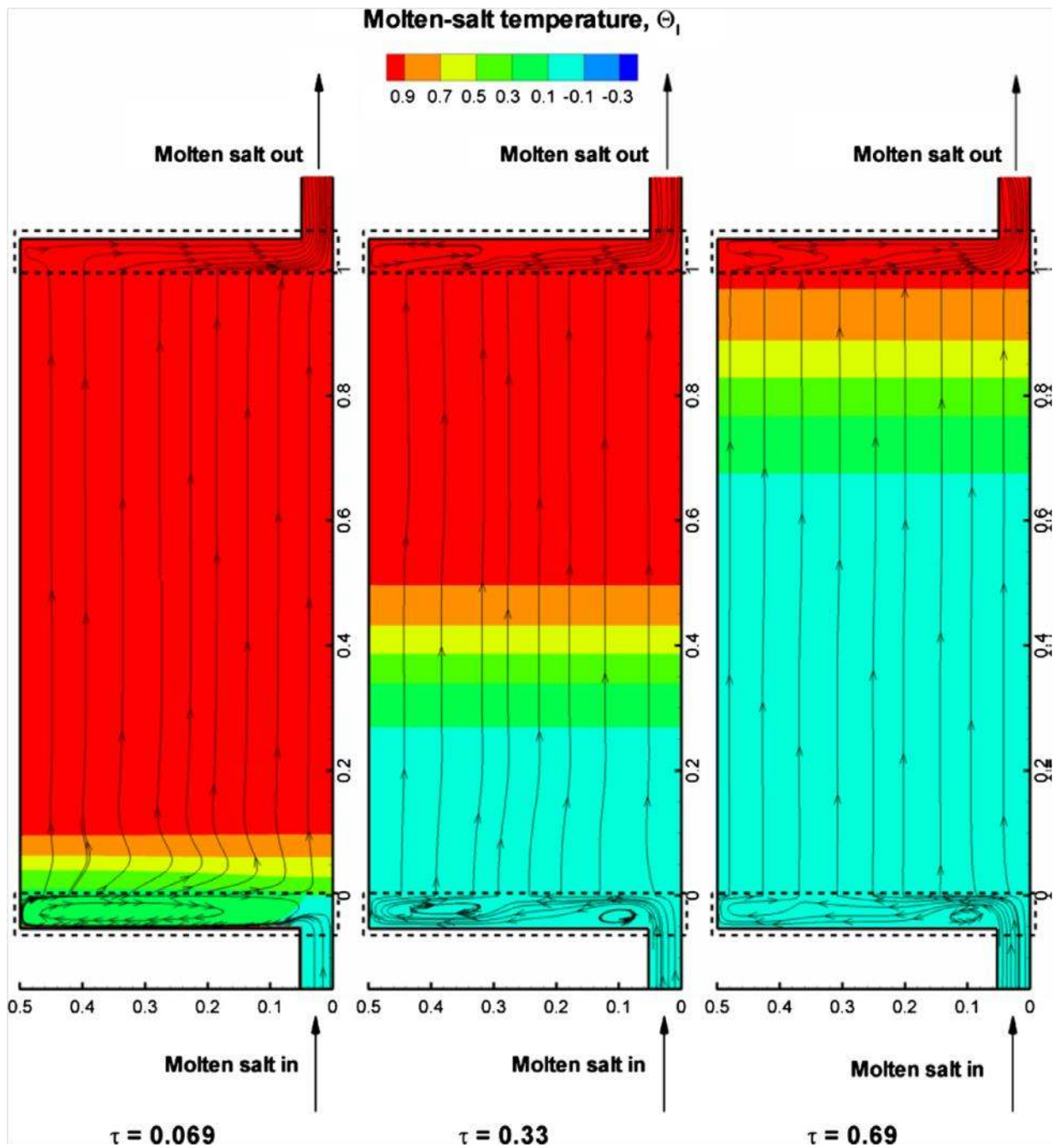
Figure 6 Flow streamlines and temperature contours in the thermocline tank (only half the tank displayed due to symmetry) with an adiabatic boundary at the tank wall (reproduced from [21]).
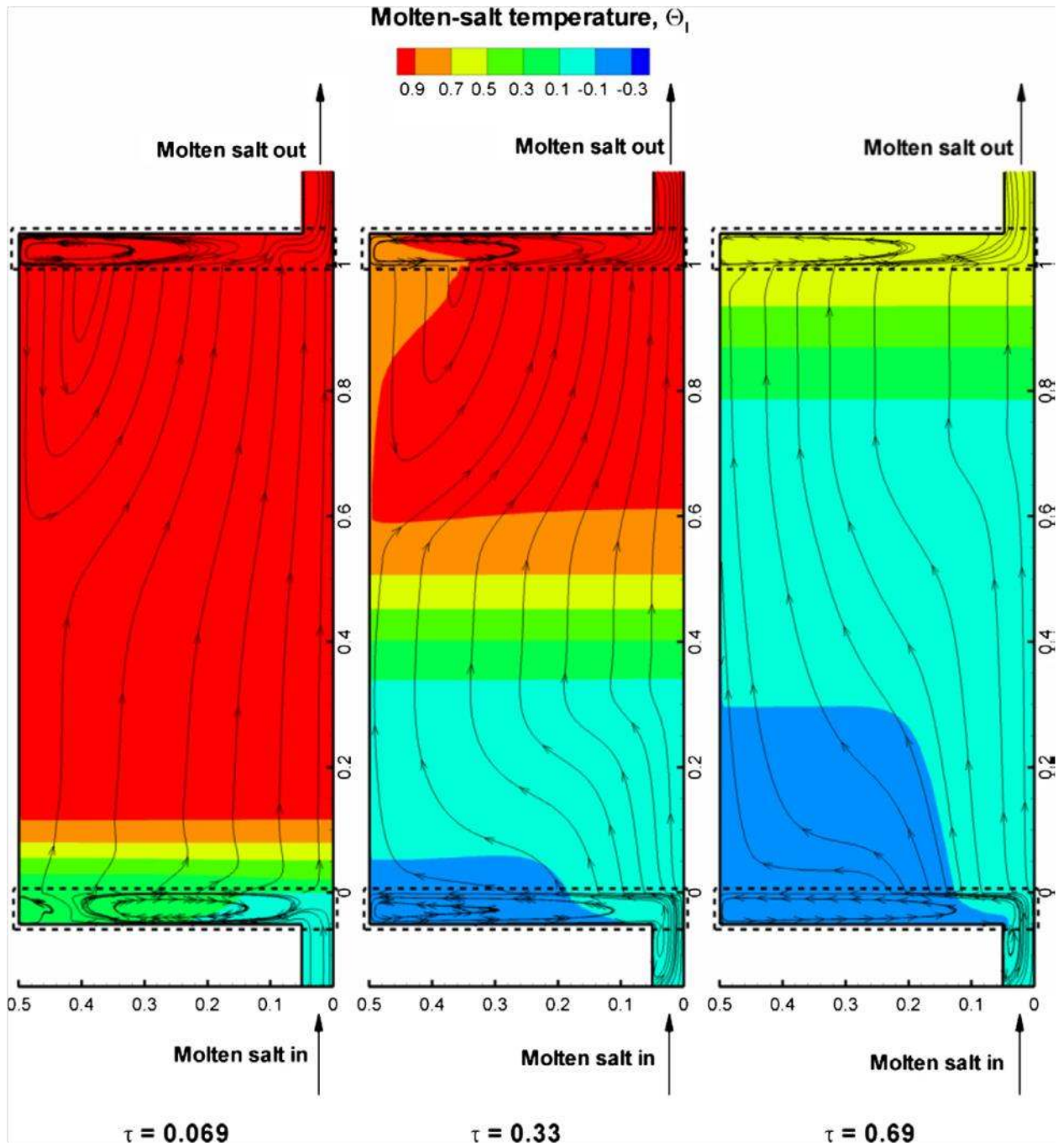
Figure 7 Flow streamlines and temperature contours in the thermocline tank with a non-adiabatic

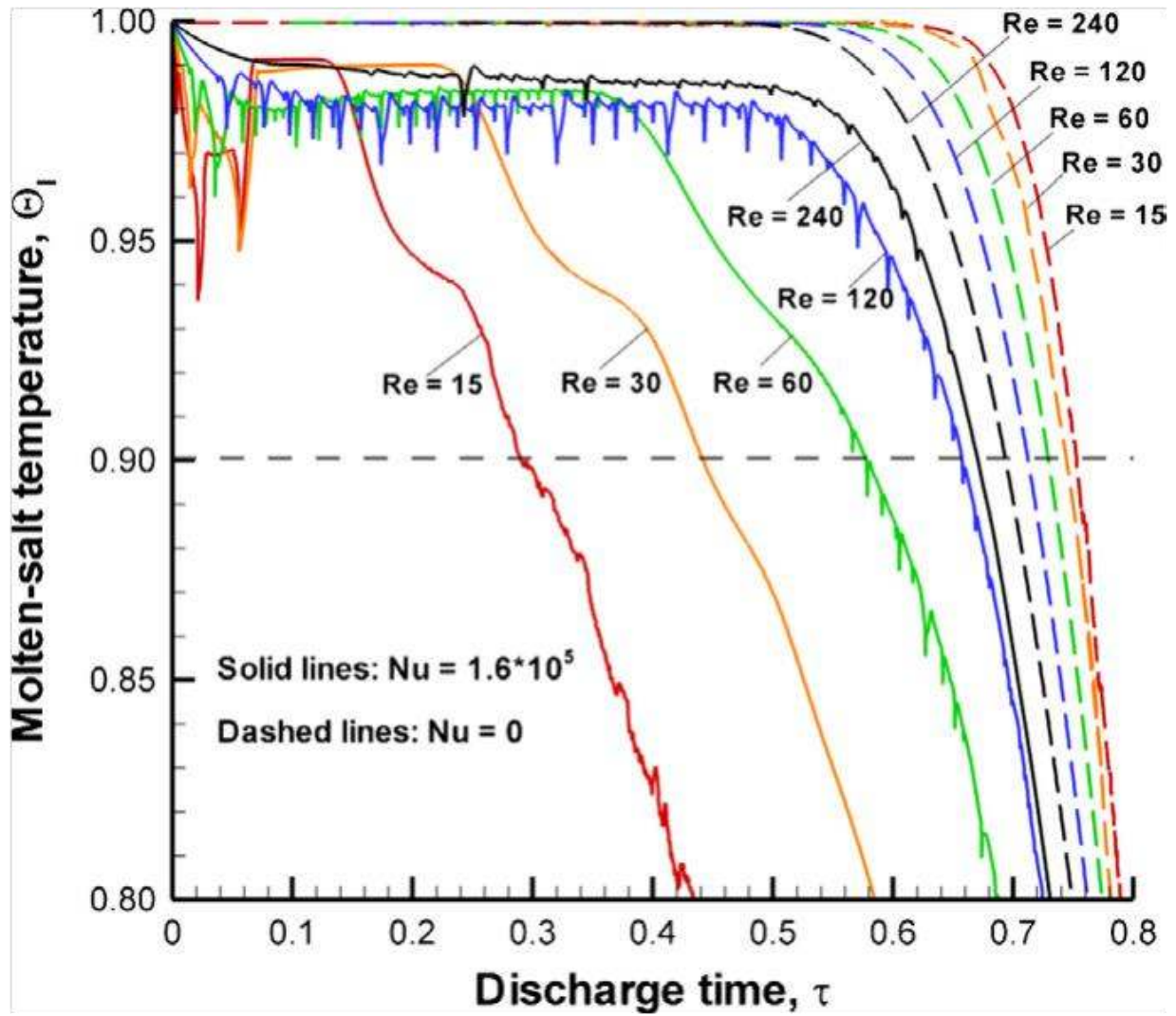boundary at the tank wall ($Nu_w = 1.6 \times 10^5$) (reproduced from [21]).

Figure 8 Temperature histories of molten-salt outflows at the top port of the tank during a discharge process. Solid lines are for a non-adiabatic wall ($Nu_w = 1.6 \times 10^5$) while dashed lines indicate an adiabatic wall ($Nu_w = 0$) (reproduced from [21]).

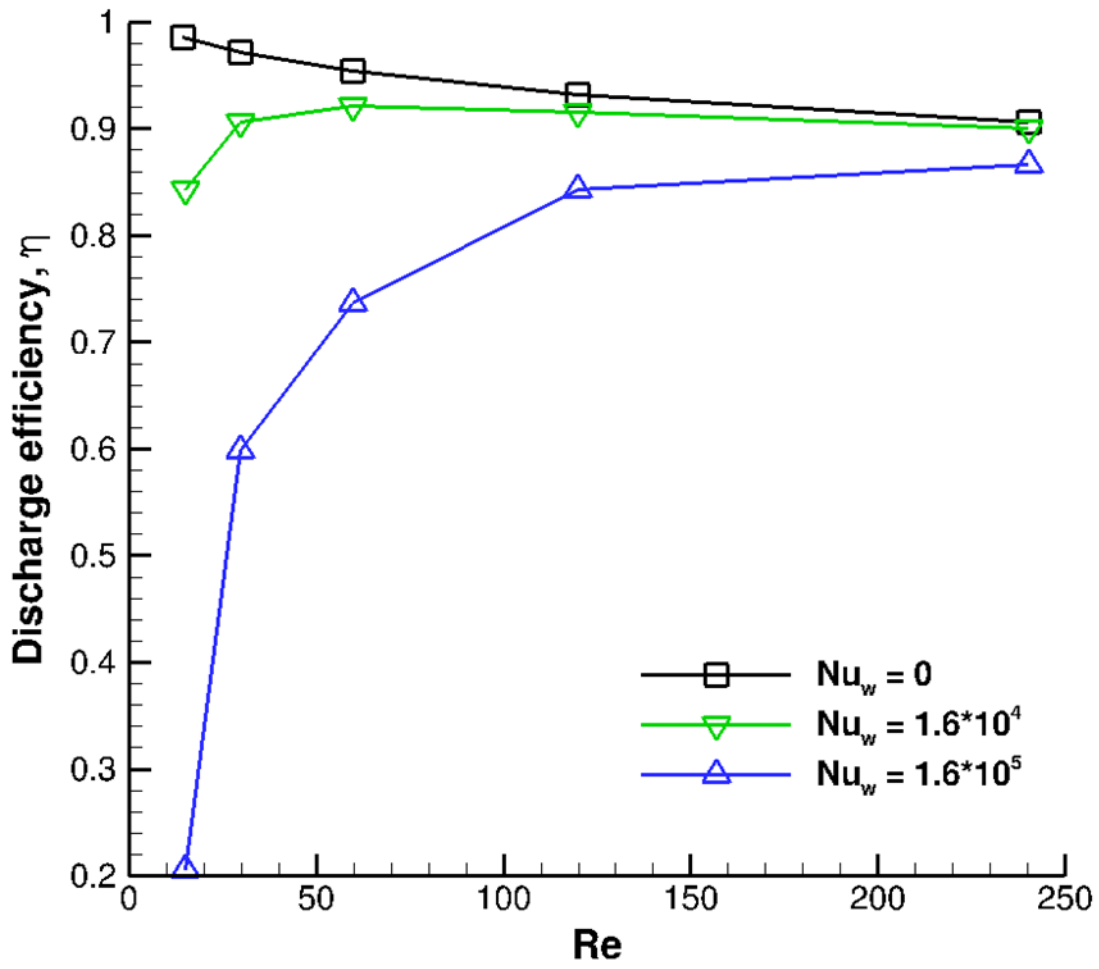Figure 9 Discharge efficiency η as a function of Re under different wall heat transfer rates
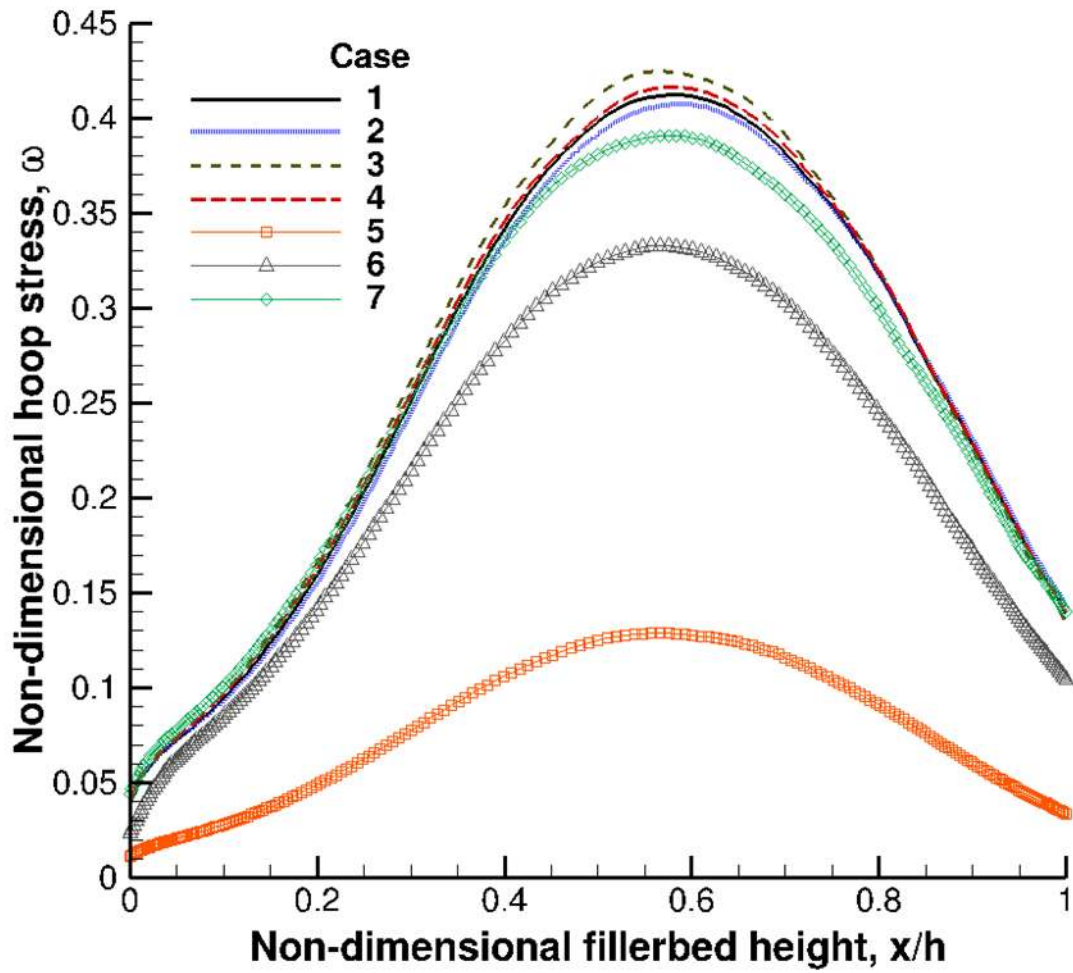
represented by Nu_w.

Figure 10 Hoop stress profiles along the fillerbed height for all cases in Table 2.